FACTA UNIVERSITATIS
Series: **Mechanical Engineering**
https://doi.org/10.22190/FUME250731034X

Original scientific paper

FAULT-TOLERANT CONTROL OF LOW-ALTITUDE UNMANNED AERIAL VEHICLE SWARMS USING A REDUCED-ORDER SLIDING MODE OBSERVER

Li Xu

School of Electronic and Information Engineering,
Ningbo University of Technology, Ningbo, China

Abstract. *The operational demands placed on unmanned aerial vehicles (UAVs) have increased significantly, rendering single low-altitude UAVs insufficient for addressing complex missions and navigating dynamically evolving information environments. To overcome these limitations, the deployment of low-altitude UAV swarms was adopted, offering enhanced agility, adaptability, and scalability. However, the expansion in swarm size leads to a higher probability of actuator faults and increased complexity in fault diagnosis and mitigation. In this study, a fault-tolerant control framework was proposed for low-altitude UAV swarms, incorporating a reduced-order sliding mode observer for real-time fault detection and isolation. A dynamic model of the UAV swarm was first established based on Newtonian mechanics and coordinate transformation techniques, accurately capturing inter-agent dynamics and external disturbances. Building upon this model, a reduced-order sliding mode observer was constructed to enable prompt estimation of actuator faults while ensuring robustness against uncertainties and model inaccuracies. Fault estimates obtained in real time were subsequently utilized in the design of a fault compensation controller to maintain swarm stability and performance in the presence of partial actuator failures. The stability and reachability of the proposed observer were rigorously validated through Lyapunov-based analysis, ensuring convergence of the fault estimation error. To evaluate the proposed methodology, an experimental UAV swarm platform operating at low altitude was developed. Experimental results demonstrate the high accuracy, resilience, and computational efficiency of the fault-tolerant control system under various fault scenarios, highlighting its practical applicability to real-world UAV swarm deployments. The proposed framework offers a scalable and robust solution for maintaining mission continuity in safety-critical UAV swarm operations.*

Key words: *Unmanned aerial vehicle swarm, Mathematical model, Sliding mode observer, Fault-tolerant control, Lyapunov stability theorem*

Received: July 31, 2025 / Accepted December 21, 2025
Corresponding author: Li Xu
School of Electronic and Information Engineering, Ningbo University of Technology, Ningbo 315211, China
E-mail: xuli@nbut.edu.cn

1. INTRODUCTION

In recent years, UAVs have been widely used in wide-area searches, low-altitude exploration, forest fire monitoring and other fields. A single UAV can hardly meet the needs of the increasingly complex information environment, and UAV swarms are becoming a research hotspot in various countries [1-5]. UAV swarms replace the individual units in a collaborative manner, which can significantly improve mission coverage and search efficiency without increasing costs [6, 7]. On the other hand, the UAV itself is a nonlinear, multiple-input multiple-output (MIMO), strongly coupled underactuated system, and the design of a single UAV control algorithm has been very complicated. Due to the geometric increase in the number of components, the fault incidence of multiple UAVs will be greatly increased. Therefore, it is a meaningful issue to consider the coordination and fault tolerance of multiple UAVs after partial faults. However, the coordination of UAVs under partial faults and their formation control design are still one of the challenges in this field [8].

In recent years, many researchers have developed many practical strategies for the collaborative formation control of UAV swarms. Dong et al. [9] presented an improved distributed control strategy for formation maneuverability and verified its effectiveness through experiments. Liao et al. [10] put forward a control scheme to produce a collision avoidance mechanism so that the UAV swarms can complete formation and reconstruction without internal collision. Kang et al. [11] developed a distance-based continuous formation control method. Belkadi et al. [12] proposed a distributed path planning strategy under the framework of multi-agent systems. Yang et al. [13] presented a UAV swarm power control method and trajectory planning derived from a depth deterministic strategy gradient. Liu et al. [14] came up with a multi-objective optimization model of UAV swarm trajectory using the decomposition method and trajectory search. However, the control schemes raised in some studies [9-14] stem from a necessary assumption, i.e., a single UAV in a UAV swarm can be regarded as an ideal particle or there are no uncertain factors such as faults and interference in each single UAV system, which is difficult to guarantee in practical applications.

In practice, one or more individuals in the low-altitude UAV swarm system inevitably receive environmental disturbance or may have actuator failures. These disturbances may spread to other individuals through the UAV network, and in severe cases, a chain reaction will be triggered, resulting in collision or misidentification between each other, where the advantages of the UAV swarm may become the cause of a serious accident [15-17]. However, as the number of the low-altitude UAVs in the formation increases, the possibility of actuator failure will be greatly improved. The UAV swarm is essentially a strongly coupled nonlinear multi-agent system, which makes its fault diagnosis and fault-tolerant control a significant challenge.

In recent years, the fault-tolerant control of a single UAV has seen great progress by using passive or active fault-tolerant technology. Aiming at the actuator fault problem of a UAV, Hasanshahi et al. [18] designed a robust fault-tolerant controller by modeling the nonlinear dynamics as an LPV system and incorporating adaptive fault estimation, thereby achieving trajectory tracking under faulty conditions. Yang et al. [19] combined the model reference adaptive control method with the fractional order method to offset the impact of actuator failure and mass change on the UAV. Liu et al. [20] developed a fault-tolerant tracking robust controller of the UAV with uncertain parameters based on a fixed-time

interference observer, and the proposed control strategy is feasible and effective in terms of disturbance suppression, fault tolerance, buffeting suppression and non-heteronormality. Wang et al. [21] developed a robust fault-tolerant controller according to the hierarchical distributed comprehensive theory, aiming at the possible external disturbance, actuator failure and wireless network-associated failure during UAV operation. Liu et al. [22] presented a fault-tolerant control scheme based on neural networks by taking advantage of the strong approximation of radial basis function neural networks to compensate for the effects of parameter uncertainties, external disturbances, and actuator faults. However, the above studies are all aimed at the failure of a single UAV, which is insufficient for the overall risk control of modern large-scale UAV formations. In recent years, some scholars have conducted a preliminary exploration on the fault-tolerant control of UAV swarms. Yu et al. [23] used sliding mode control and model reference adaptive control to compensate for the impact of actuator faults on UAV swarms, but it belongs to passive fault-tolerant control and lacks fault diagnosis. Reppa et al. [24] established the diagnosis and isolation of UAV swarm faults through multi-sensor fusion and applied a global decision logic, but failed to compensate for the faults.

From the above analysis, it can be learned that the research on fault diagnosis and fault-tolerant control of a single UAV has led to many important achievements, but there is still an open challenge for the research of low-altitude UAV swarms. The fault-tolerant control difference between a single UAV and UAV swarms can be summarized as follows: a) The controller of the UAV swarm consists of an outer-loop group controller and an inner-loop individual UAV controller. The output of the inner-loop individual UAV controller serves as the input for the outer-loop group controller. Faults can propagate through the inner and outer control loops; hence, the fault diagnosis and fault-tolerant control of the UAV swarm must consider not only the impact of faults on the individual UAV but also their effects on the entire group. b) In a UAV swarm, in addition to individual UAV malfunctions, there can also be communication failures between UAVs. Moreover, these communication failures can be amplified as information is passed between UAVs. Therefore, fault diagnosis and fault-tolerant control require the establishment of a global error system for the UAV swarm to estimate and compensate for these faults.

To address the two key research gaps for low-altitude drone swarms mentioned above, the novelty of our work lies in:

1) The fault-tolerant control method with active compensation that enhances formation stability in the event of actuator failure.

2) The designed reduced-order sliding mode observer for fault estimation that enables more efficient fault detection and thus enhances system stability.

3) The framework capable of handling effectively multiple actuator failures and maintaining swarm formation stability under disturbances.

The rest of this study is organized as follows. In Section 2, the position relationship of adjacent wingmen in the low-altitude UAV swarm was analyzed, and the formation model of the inner and outer-loop UAV swarm under the wingman strategy was established. In Section 3, a sliding mode observer with reduced order was designed for fault diagnosis, and its reachability and stability were proved. In Section 4, the estimated faults and disturbances were solved by using the sliding mode observer, and active fault-tolerant control was carried out to realize the trajectory tracking in the case of actuator faults. In Section 5, the effectiveness of the developed method was verified by experiments. Section 6 summarizes the content of the study.

2. CONSTRUCTION OF THE UAV CLUSTER MODEL

2.1 Construction of a Single UAV Motion Model

Assuming the Earth's curvature is neglected and the ground coordinate system is adopted as the inertial coordinate system, the definitions of the ground reference frame and the body reference frame are illustrated in Fig. 1, with specific details as follows:

(1) **Ground coordinate system** S_g-$Oxyz$: The origin O is a selected point on the ground. The x-axis lies in the horizontal plane and points in a specific direction; the z-axis is perpendicular to the ground and points toward the Earth's center; the y-axis also lies in the horizontal plane, is perpendicular to the x-axis, and is determined in accordance with the right-hand rule.

(2) **Body coordinate system** S_b-$O_bx_by_bz_b$: The origin O_b is located at the center of mass of the unmanned aerial vehicle (UAV) and is fixed to the aircraft. The x_b-axis lies in the aircraft's plane of symmetry, is parallel to the aircraft's design axis, and points toward the nose. The y_b-axis is perpendicular to the aircraft's plane of symmetry and points toward the right side of the fuselage. The z_b-axis lies in the aircraft's plane of symmetry, is perpendicular to the x_b-axis, and points toward the bottom of the fuselage.

(3) **Aircraft attitude angles** are determined by the relationship between the body coordinate system and the ground coordinate system, which are known as Euler angles. Specifically:

- The **pitch angle** θ is the angle between the body axis x_b and the horizontal plane, with a positive value corresponding to the nose-up attitude.
- The **yaw angle** ψ is the angle between the projection of the body axis x_b onto the horizontal plane and the ground axis x, with a positive value corresponding to the nose yawing to the right.
- The **roll angle** ϕ is the angle between the body axis z_b and the vertical plane passing through the body axis x_b, with a positive value corresponding to the aircraft rolling to the right.

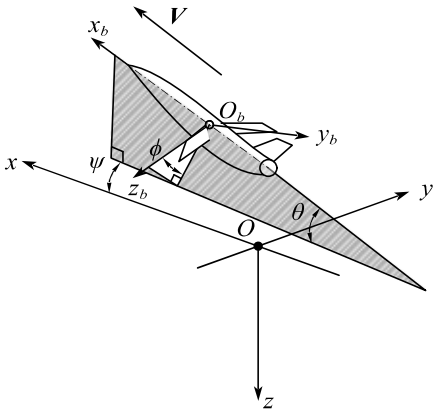

Fig. 1 The relationship between the body coordinate system S_b and the ground coordinate system S_g

Newton's second law can be applied to establish the linear motion and angular motion dynamics equations of a single UAV under the action of the external force $\boldsymbol{F}$ and the external torque $\boldsymbol{M}$.

The linear motion dynamics equation of a UAV with the external force $\boldsymbol{F}$ can be expressed as follows:

$$\sum \boldsymbol{F} = m\frac{\mathrm{d}\boldsymbol{V}}{\mathrm{d}t} \tag{1}$$

where $\boldsymbol{V}$ denotes the velocity vector of the UAV's center of mass, t denotes the time and m denotes the mass of the UAV.

The angular motion dynamics equation of a UAV under the action of the external torque $\boldsymbol{M}$ can be expressed as:

$$\sum \boldsymbol{M} = \frac{\mathrm{d}\boldsymbol{L}}{\mathrm{d}t} \tag{2}$$

where $\boldsymbol{L}$ is the moment of momentum. To establish the relative motion relationship of the UAV relative to the ground coordinate system, the body coordinate system was selected to establish the dynamic coordinate system. Assuming that the velocity of the body coordinate system relative to the inertial coordinate system is $\boldsymbol{V}$ and the angular velocity vector is $\boldsymbol{\Omega}$, then it can be written:

$$\frac{\mathrm{d}\boldsymbol{V}}{\mathrm{d}t} = \boldsymbol{I}_V \frac{\delta \boldsymbol{V}}{\delta t} + \boldsymbol{\Omega} \times \boldsymbol{V} \tag{3}$$

$$\frac{\mathrm{d}\boldsymbol{L}}{\mathrm{d}t} = \boldsymbol{I}_L \frac{\delta \boldsymbol{L}}{\delta t} + \boldsymbol{\Omega} \times \boldsymbol{L} \tag{4}$$

where $\boldsymbol{I}_V$ and $\boldsymbol{I}_L$ are the unit vectors along the flight speed $\boldsymbol{V}$ and the moment of momentum $\boldsymbol{L}$, respectively, $\frac{\delta \boldsymbol{V}}{\delta t}$ and $\frac{\delta \boldsymbol{L}}{\delta t}$ represent the relative derivatives in the dynamic coordinate system, and $\boldsymbol{\Omega}$ is the total angular velocity vector in the dynamic coordinate system relative to the inertial coordinate system.

$\boldsymbol{V}$ and $\boldsymbol{\Omega}$ can be represented via their components, as follows:

$$\boldsymbol{V} = \boldsymbol{i}u + \boldsymbol{j}v + \boldsymbol{k}w \tag{5}$$

$$\boldsymbol{\Omega} = \boldsymbol{i}p + \boldsymbol{j}q + \boldsymbol{k}r \tag{6}$$

where $\boldsymbol{i}$, $\boldsymbol{j}$ and $\boldsymbol{k}$ are the unit vectors in the directions of the x-axis, y-axis and z-axis, respectively; u, v and w represent the velocity $\boldsymbol{V}$ components along the x_b-axis, y_b-axis and z_b-axis, respectively, and p, q, and r represent the components of the rotational angular velocity $\boldsymbol{\Omega}$ of the aircraft coordinate system relative to the ground coordinate system on the x_b-axis, y_b-axis and z_b-axis of the aircraft coordinate system, respectively.

In what follows, Eq. (3) can be adequately rewritten. The first term on the right-hand side of Eq. (3) reads:

$$\boldsymbol{I}_V \frac{\delta \boldsymbol{V}}{\delta t} = \boldsymbol{i}\frac{\delta u}{\delta t} + \boldsymbol{j}\frac{\delta v}{\delta t} + \boldsymbol{k}\frac{\delta w}{\delta t} = \boldsymbol{i}\dot{u} + \boldsymbol{j}\dot{v} + \boldsymbol{k}\dot{w} \tag{7}$$

The second item on the right-hand side of Eq. (3) is:

$$\boldsymbol{\Omega} \times \boldsymbol{V} = \begin{vmatrix} \boldsymbol{i} & \boldsymbol{j} & \boldsymbol{k} \\ p & q & r \\ u & v & w \end{vmatrix} = (wq - vr)\boldsymbol{i} + (ur - wp)\boldsymbol{j} + (vp - uq)\boldsymbol{k} \tag{8}$$

The combined force can also be represented via its components:

$$\sum \boldsymbol{F} = \boldsymbol{i}F_{x_b} + \boldsymbol{j}F_{y_b} + \boldsymbol{k}F_{z_b} \tag{9}$$

where F_{x_b}, F_{y_b} and F_{z_b} are the resultant components along each axis.

From Eqs. (7)-(9) and Eq. (1), one may write:

$$\left.\begin{aligned} F_{x_b} &= m(\dot{u} - vr + wq) \\ F_{y_b} &= m(\dot{v} - wp + ur) \\ F_{z_b} &= m(\dot{w} - uq + vp) \end{aligned}\right\} \tag{10}$$

Unless otherwise specified, a dot above a variable in the text indicates the derivative of that variable with respect to time.

In the UAV system, considering the combined forces of the total aerodynamic force and engine thrust on various coordinates F_{x_b}, F_{y_b} and F_{z_b}, gravity g is represented via its components with respect to the dynamic coordinate system. Eq. (10) can be then rewritten as follows [25]:

$$\left.\begin{aligned} \dot{u} &= vr - g\sin\theta - wq + \frac{F_{x_b}}{m} \\ \dot{v} &= wq - ur + g\sin\phi\cos\theta + \frac{F_{y_b}}{m} \\ \dot{w} &= uq - vp + g\cos\phi\cos\theta + \frac{F_{z_b}}{m} \end{aligned}\right\} \tag{11}$$

The resulting Eq. (11) represents the linear motion dynamics model of the UAV. Similarly, considering the angular motion dynamics model of the UAV, Eq. (4) can be suitably rewritten as it will be demonstrated below.

The first term on the right-hand side of Eq. (4) is:

$$\boldsymbol{I}_L \frac{\delta \boldsymbol{L}}{\delta t} = \boldsymbol{i}\frac{\delta L_{x_b}}{\delta t} + \boldsymbol{j}\frac{\delta L_{y_b}}{\delta t} + \boldsymbol{k}\frac{\delta L_{z_b}}{\delta t} \tag{12}$$

where L_{x_b}, L_{y_b} and L_{z_b} denote the components of the moment of momentum with respect to the x_b-axis, y_b-axis and z_b-axis, respectively. The right hand-side of the equation can be decomposed into:

$$\left.\begin{aligned} \frac{\delta L_{x_b}}{\delta t} &= \dot{p} I_{x_b} - \dot{r} I_{x_b z_b} \\ \frac{\delta L_{y_b}}{\delta t} &= \dot{q} I_{y_b} \\ \frac{\delta L_{z_b}}{\delta t} &= \dot{r} I_{z_b} - \dot{p} I_{x_b z_b} \end{aligned}\right\} \tag{13}$$

where I_{x_b}, I_{y_b} and I_{z_b} are the moments of inertia of the UAV with respect to the x_b-axis, y_b-axis and z_b-axis, respectively, and $I_{x_b z_b}$ is the product of inertia of the UAV with respect to the x_b-axis and z_b -axis.

The second term on the right-hand side of Eq. (4) can be rewritten as follows:

$$\boldsymbol{\Omega} \times \boldsymbol{L} = \begin{vmatrix} \boldsymbol{i} & \boldsymbol{j} & \boldsymbol{k} \\ p & q & r \\ L_{x_b} & L_{y_b} & L_{z_b} \end{vmatrix} = \boldsymbol{i}(qL_{z_b} - rL_{y_b}) + \boldsymbol{j}(rL_{x_b} - pL_{z_b}) + \boldsymbol{k}(pL_{y_b} - qL_{x_b}) \tag{14}$$

By decomposing the combined torque into each axis of the dynamic coordinate system and synthesizing Eq. (2) and Eqs. (12-14), the angular motion dynamics equation of the UAV can be obtained:

$$\begin{cases} \dot{p} = [I_{z_b} M_{x_b} + I_{x_b z_b} M_{z_b} - (I_{z_b}^2 + I_{x_b z_b}^2 - I_{y_b} I_{z_b}) qr + I_{x_b z_b} (I_{x_b} - I_{y_b} + I_{z_b} pq)] / (I_{x_b} I_{z_b} - I_{x_b z_b}^2) \\ \dot{q} = [-pr(I_{x_b} - I_{z_b}) + M_{y_b} + I_{x_b z_b} (p^2 - r^2)] / I_{y_b} \\ \dot{r} = [I_{x_b z_b} M_{x_b} + I_{x_b} M_{z_b} + (I_{x_b}^2 + I_{x_b z_b}^2 - I_{x_b} I_{y_b}) pq - I_{x_b z_b} (I_{x_b} - I_{y_b} + I_{z_b}) qr] / (I_{x_b} I_{z_b} - I_{x_b z_b}^2) \end{cases} \tag{15}$$

where M_{x_b}, M_{y_b} and M_{z_b} are the torque components about the x_b-, y_b-, and z_b-axis, respectively.

Eqs. (11)-(15) constitute the dynamic model of a UAV. To further describe the motion of the UAV, a kinematic model needs to be constructed. In the inertial system, it can be obtained from geometric relationships:

$$\begin{cases} \dot{\phi} = q \tan\theta \sin\phi + r \tan\theta \cos\phi + p \\ \dot{\theta} = -r \sin\phi + q \cos\phi \\ \dot{\psi} = (r \cos\phi + q \sin\phi) / \cos\theta \end{cases} \tag{16}$$

Eqs. (11), (15) and (16) establish the complete motion model (including dynamics and kinematics) of a single UAV, which is the six-degree-of-freedom nonlinear equation of the UAV.

Using [*u, v, w, p, q, r, θ, ψ, ϕ*] as a state variable, the model can be written in the form of a state space. Due to the nonlinear relationship in the motion model and the close correlation between force and torque and motion parameters, it is difficult to obtain analytical solutions, and numerical solutions can only be obtained with the help of computers. Therefore, the model obtained after partial linearization using the small perturbation principle is as follows [26, 27]:

$$\begin{cases} \dot{\boldsymbol{x}}(t) = \boldsymbol{A}\boldsymbol{x}(t) + \boldsymbol{G}(\boldsymbol{x}(t), \boldsymbol{u}(t)) \\ \boldsymbol{y}(t) = \boldsymbol{C}\boldsymbol{x}(t) \end{cases} \tag{17}$$

where $\boldsymbol{x}(t) = [u, v, w, p, q, r, \theta, \psi, \phi]^{\mathrm{T}}$ is the state variable of the system, $\boldsymbol{u}(t) = [\delta_e, \delta_t, \delta_a, \delta_r]^{\mathrm{T}} = [\mathrm{u1,u2,u3,u4}]^{\mathrm{T}}$ is the input of the system, being the elevator, throttle, flaps, and ailerons; $\boldsymbol{y}(t)$ is the output vector of the system; $\boldsymbol{G}(\boldsymbol{x}(t),\boldsymbol{u}(t))$ is the nonlinear vector function; $\boldsymbol{A}$ and $\boldsymbol{C}$ are the coefficient matrices after linearization.

Assuming that the nonlinear part of $\boldsymbol{G}(\boldsymbol{x}(t),\boldsymbol{u}(t))$ is independent of the control input $\boldsymbol{u}(t)$, Eq. (17) can be decoupled into the form of $\boldsymbol{B}\boldsymbol{u}(t) + \boldsymbol{g}(\boldsymbol{x}(t))$, where $\boldsymbol{g}(\boldsymbol{x}(t))$ is a continuous nonlinear function that satisfies the Lipschitz condition.

2.2 Construction of the UAV Cluster Motion Model

The motion model construction of a single UAV was completed in Section 2.1. Now the UAV cluster model under the lead wingman strategy in the planar coordinate system is considered, as shown in Fig. 2.

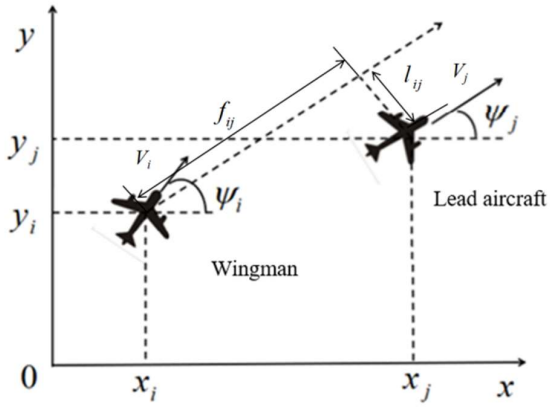

Fig.2 Schematic diagram of the UAV formation under the lead wingman strategy

According to the geometric relationship in the figure, the motion equation of the i-th UAV can be obtained as follows:

$$\begin{cases} \dot{x}_i = V_i \cos\psi_i \\ \dot{y}_i = V_i \sin\psi_i \\ \dot{\psi}_i = \omega_i \end{cases} \tag{18}$$

where the planar coordinate system is composed of the x-axis and y-axis defined in Section 2.1 of the ground coordinate system, x_i, y_i represent the position of the i-th UAV, V_i, ω_i represent the forward and angular velocities of the i-th UAV, and ψ_i denotes the angle between the forward velocity of the i-th UAV and the x-axis.

Fig. 1 shows that the relative forward distance f_{ij} and the lateral distance l_{ij} between the lead aircraft and the wingman could be expressed as:

$$\begin{aligned} f_{ij} &= (y_i - y_j)\sin\psi_j + (x_i - x_j)\cos\psi_j + d\cos(\psi_i - \psi_j) \\ l_{ij} &= -(y_i - y_j)\cos\psi_j + (x_i - x_j)\sin\psi_j - d\sin(\psi_i - \psi_j) \end{aligned} \tag{19}$$

where d denotes the distance between the control and actual centers [28, 29]. The forward error $e_{f_{ij}}$ and the lateral error $e_{l_{ij}}$ between the forward and lateral distances, as well as the expected forward and lateral distances, can be written as a state space expression to obtain:

$$\begin{bmatrix} \dot{e}_{f_{ij}} \\ \dot{e}_{l_{ij}} \end{bmatrix} = \begin{bmatrix} -V_j - l_{ij}\omega_j \\ f_{ij}\omega_j \end{bmatrix} + \begin{bmatrix} \cos(\psi_i - \psi_j) & -d\sin(\psi_i - \psi_j) \\ -\sin(\psi_i - \psi_j) & -d\cos(\psi_i - \psi_j) \end{bmatrix} \begin{bmatrix} V_i \\ \omega_i \end{bmatrix} \tag{20}$$

Comparing Eqs. (18) and (20), it can be seen that the output of the kinematic model of a single UAV is the input of the kinematic model of the UAV cluster.

2.3 Construction of the UAV Motion Model in the Presence of Faults

To construct a fault model for the UAV cluster, it can be assumed that one or more UAVs have malfunctioned, i.e., the i-th UAV has malfunctioned. The motion model of a single UAV given in Eq. (17) can be rewritten as:

$$\begin{cases} \dot{\boldsymbol{x}}_i(t) = \boldsymbol{A}_i\boldsymbol{x}_i(t) + \boldsymbol{B}_i\boldsymbol{u}_i(t) + \boldsymbol{g}(\boldsymbol{x}_i(t)) + \boldsymbol{D}_i\boldsymbol{\Phi}_i(t) + \boldsymbol{E}_i\boldsymbol{f}_i(t) \\ \boldsymbol{y}_i(t) = \boldsymbol{C}_i\boldsymbol{x}_i(t) \end{cases} \tag{21}$$

where $\boldsymbol{\Phi}_i(t)$ represents the unknown nonlinear disturbance and parameter uncertainty of the system, and $\boldsymbol{f}_i(t)$ denotes the unknown fault term of the system that occurred on the i-th UAV, $\boldsymbol{D}_i$ and $\boldsymbol{E}_i$ are the time-invariant coefficient matrices.

3. Sliding Mode Observer and Fault-Tolerant Controller Design

The outer-loop UAV group control system needs to be designed. The reconstruction can be obtained as follows:

$$\begin{aligned} \begin{bmatrix} \dot{e}_{f_{ij}} \\ \dot{e}_{l_{ij}} \end{bmatrix} &= \begin{bmatrix} -V_j - l_{ij}\omega_j \\ f_{ij}\omega_j \end{bmatrix} + \begin{bmatrix} \cos(\psi_i - \psi_j) & -d\sin(\psi_i - \psi_j) \\ -\sin(\psi_i - \psi_j) & -d\cos(\psi_i - \psi_j) \end{bmatrix} \begin{bmatrix} V_i^* \\ \omega_i^* \end{bmatrix} \\ &+ \begin{bmatrix} \cos(\psi_i - \psi_j) & -d\sin(\psi_i - \psi_j) \\ -\sin(\psi_i - \psi_j) & -d\cos(\psi_i - \psi_j) \end{bmatrix} \begin{bmatrix} V_i - V_i^* \\ \omega_i - \omega_i^* \end{bmatrix} \end{aligned} \tag{22}$$

where V_i^* and ω_i^* are the expected forward and angular velocities of the i-th UAV. To make the system stable, the introduction of a Proportional-Integral (PI) control rate can be derived as follows:

$$\begin{bmatrix} \dot{e}_{f_{ij}} \\ \dot{e}_{l_{ij}} \end{bmatrix} = \begin{bmatrix} -(K_{P1}e_{f_{ij}} + K_{I1}\int e_{f_{ij}}\,dt) \\ -(K_{P2}e_{l_{ij}} + K_{I2}\int e_{l_{ij}}\,dt) \end{bmatrix} + \begin{bmatrix} \cos(\psi_i - \psi_j) & -d\sin(\psi_i - \psi_j) \\ -\sin(\psi_i - \psi_j) & -d\cos(\psi_i - \psi_j) \end{bmatrix} \begin{bmatrix} V_i - V_i^* \\ \omega_i - \omega_i^* \end{bmatrix} \tag{23}$$

where K_{Pi}, K_{Ii}, i=1, 2 respectively represent the proportional gain and integral gain of the

PI control law.

When V_i^*, ω_i^* and V_i, ω_i are equal, i.e., when the UAV tracks the desired signal, the following can be obtained:

$$\begin{bmatrix} \dot{e}_{f_{ij}} \\ \dot{e}_{l_{ij}} \end{bmatrix} = \begin{bmatrix} -(K_{P1}e_{f_{ij}} + K_{I1}\int e_{f_{ij}}dt) \\ -(K_{P2}e_{l_{ij}} + K_{I2}\int e_{l_{ij}}dt) \end{bmatrix} \tag{24}$$

Obviously, Eq. (24) is asymptotically stable, which means that when each UAV in the UAV group is stable under normal or fault conditions, the stability of the UAV group can be guaranteed.

To ensure that the state variables of the inner-loop UAV can track their reference values, a sliding mode tracking controller for the inner-loop UAV was designed.

Assumption 1. For the nonlinear term in the nonlinear model of a single UAV in Eq. (17), there is a continuous bounded function $\boldsymbol{\lambda}(\boldsymbol{x}_i(t)) > 0$ such that it can satisfy the following inequality:

$$\left\| \boldsymbol{S}_i^T \boldsymbol{L}_i \boldsymbol{C} \boldsymbol{g}(\boldsymbol{x}_i(t)) \right\| \le \boldsymbol{\lambda}(\boldsymbol{x}_i(t)) \left\| \boldsymbol{S}_i^T \boldsymbol{L}_i \boldsymbol{C} \boldsymbol{B} \right\| \tag{25}$$

where $\boldsymbol{S}_i$ is the sliding surface.

The sliding surface of the sliding mode tracking controller of the inner-loop UAV was designed as follows:

$$\boldsymbol{S}_i = \boldsymbol{e}_{yi} + \boldsymbol{K}_i \int_0^t \boldsymbol{e}_{yi} dt = 0 \tag{26}$$

where $\boldsymbol{e}_{yi} = \boldsymbol{y}_{ri} - \boldsymbol{L}_i \boldsymbol{y}_i$ represents the output tracking error of the i-th UAV, $\boldsymbol{y}_{ri}$ denotes the expected output of the i-th UAV, $\boldsymbol{y}_i$ denotes the actual output of the i-th UAV, and $\boldsymbol{L}_i$ represents the dimension adaptation matrix. The following derivation of Eq. (26) can be obtained:

$$\dot{\boldsymbol{S}}_i = \dot{\boldsymbol{e}}_{yi} + \boldsymbol{K}_i \boldsymbol{e}_{yi} = \dot{\boldsymbol{y}}_{ri} - \boldsymbol{L}_i \boldsymbol{C} \dot{\boldsymbol{x}}_i + \boldsymbol{K}_i \boldsymbol{e}_{yi} \tag{27}$$

Its stability was proved below. A Lyapunov function V_i was considered as follows:

$$V_i = \frac{1}{2} \boldsymbol{S}_i^T \boldsymbol{S}_i \tag{28}$$

The derivation of Eq. (28) can be obtained:

$$\dot{V}_i = \boldsymbol{S}_i^T \boldsymbol{S}_i = \boldsymbol{S}_i^T (\dot{\boldsymbol{y}}_{ri} - \boldsymbol{L}_i \boldsymbol{C} \dot{\boldsymbol{x}}_i + \boldsymbol{K}_i \boldsymbol{e}_{yi}) \tag{29}$$

To guarantee that the system can be stable on the sliding surface, i.e., $V_i < 0$, the input $\boldsymbol{u}_i = \boldsymbol{u}_{i1} + \boldsymbol{u}_{i2}$ of the controller was designed as:

$$\begin{cases} \boldsymbol{u}_{i1} = \boldsymbol{B}^T (\boldsymbol{B}\boldsymbol{B}^T)^{-1} ((\boldsymbol{L}_i \boldsymbol{C})^T ((\boldsymbol{L}_i \boldsymbol{C})(\boldsymbol{L}_i \boldsymbol{C})^T)^{-1} (\dot{\boldsymbol{y}}_{ri} + \boldsymbol{K}_i \boldsymbol{e}_{yi} + \rho_i \text{sign}(\boldsymbol{S}_i)) - \boldsymbol{A}\boldsymbol{x}_i) \\ \boldsymbol{u}_{i2} = \dfrac{\boldsymbol{\lambda}(\boldsymbol{x}_i(t))(\boldsymbol{S}_i^T \boldsymbol{L}_i \boldsymbol{C} \boldsymbol{B})^T}{\left\| \boldsymbol{S}_i^T \boldsymbol{L}_i \boldsymbol{C} \boldsymbol{B} \right\|} \end{cases} \tag{30}$$

where $\rho_i > 0$ is the designed gain, and sign($\boldsymbol{S}_i$) is the designed sign function vector. Substituting Eq. (30) into Eq. (29), the following can be obtained from Eq. (25):

$$\begin{aligned}\dot{\mathrm{V}}_i &= -\rho_i \boldsymbol{S}_i^T \operatorname{sign}(\boldsymbol{S}_i) - \boldsymbol{S}_i^T \boldsymbol{L}_i \boldsymbol{C}(\boldsymbol{B}(\frac{\boldsymbol{\lambda}(\boldsymbol{x}_i(t))(\boldsymbol{S}_i^T \boldsymbol{L}_i \boldsymbol{C}\boldsymbol{B})^T}{\left\|\boldsymbol{S}_i^T \boldsymbol{L}_i \boldsymbol{C}\boldsymbol{B}\right\|})) - \boldsymbol{S}_i^T \boldsymbol{L}_i \boldsymbol{C}\boldsymbol{g}(\boldsymbol{x}_i(t)) \\ &\le -\rho_i \boldsymbol{S}_i^T \operatorname{sign}(\boldsymbol{S}_i) - \boldsymbol{\lambda}(\boldsymbol{x}_i(t))\left\|\boldsymbol{S}_i^T \boldsymbol{L}_i \boldsymbol{C}\boldsymbol{B}\right\| + \left\|\boldsymbol{S}_i^T \boldsymbol{L}_i \boldsymbol{C}\boldsymbol{g}(\boldsymbol{x}_i(t))\right\| \\ &\le -\rho_i \sum_{n=1}^{2} \left|\boldsymbol{S}_i\right| \le 0\end{aligned} \tag{31}$$

This indicates that the system can stabilize on the sliding surface after reaching the sliding surface.

After designing the sliding mode controller, it is necessary to design a sliding mode observer to observe the fault. The reconstruction of Eq. (21) can be obtained as follows:

$$\begin{cases}\dot{\boldsymbol{x}}_{i1}(t) = \boldsymbol{A}_{11}\boldsymbol{x}_{i1}(t) + \boldsymbol{A}_{12}\boldsymbol{x}_{i2}(t) + \boldsymbol{G}_1(\boldsymbol{x}_i(t), \boldsymbol{u}_i(t)) + \boldsymbol{D}_1\boldsymbol{\Phi}_i(t) + \boldsymbol{E}_1\boldsymbol{f}_i(t) \\ \dot{\boldsymbol{x}}_{i2}(t) = \boldsymbol{A}_{21}\boldsymbol{x}_{i1}(t) + \boldsymbol{A}_{22}\boldsymbol{x}_{i2}(t) + \boldsymbol{G}_2(\boldsymbol{x}_i(t), \boldsymbol{u}_i(t)) + \boldsymbol{D}_2\boldsymbol{\Phi}_i(t) + \boldsymbol{E}_2\boldsymbol{f}_i(t) \\ \boldsymbol{y}_i(t) = \boldsymbol{x}_{i2}(t)\end{cases} \tag{32}$$

where $\boldsymbol{x}_{i1}, \boldsymbol{x}_{i2} \in R^p$ are the upper and lower parts obtained by decomposing the system state vector $\boldsymbol{x}_i$, $\boldsymbol{G}_1(\boldsymbol{x}_i(t),\boldsymbol{u}_i(t))$ and $\boldsymbol{G}_2(\boldsymbol{x}_i(t),\boldsymbol{u}_i(t))$ are the upper and lower parts obtained by decomposing $\boldsymbol{G}(\boldsymbol{x}_i(t),\boldsymbol{u}_i(t))$, $\boldsymbol{f}_i(t)$ denotes the unknown fault term of the system and has a known upper bound γ_2, $\boldsymbol{\Phi}_i(t)$ represents the unknown nonlinear disturbance and parameter uncertainty of the system, and $\boldsymbol{D}_1$,$\boldsymbol{D}_2$, $\boldsymbol{E}_1$ and $\boldsymbol{E}_2$ are the time-invariant coefficient matrices.

Assumption 2: In Eq. (21), the matrix pair ($\boldsymbol{A}$, $\boldsymbol{C}$) is detectable.

From Assumption 2, there exists a matrix $\boldsymbol{L}$ such that the matrix $\boldsymbol{A}$-$\boldsymbol{LC}$ is stable and satisfies the following Lyapunov equation:

$$(\boldsymbol{A} - \boldsymbol{L}\boldsymbol{C})^T \boldsymbol{P} + \boldsymbol{P}(\boldsymbol{A} - \boldsymbol{L}\boldsymbol{C}) = -\boldsymbol{Q} \tag{33}$$

where $\boldsymbol{Q} > 0$, and there exists a unique solution $\boldsymbol{P} > 0$ for Eq. (33).

The linear transformation $\boldsymbol{z}_i = \boldsymbol{T}\boldsymbol{x}_i$ was introduced, where:

$$\boldsymbol{T} = \begin{bmatrix} \boldsymbol{I}_{n-p} & \boldsymbol{P}_1^{-1}\boldsymbol{P}_2 \\ \boldsymbol{0} & \boldsymbol{I}_p \end{bmatrix} \tag{34}$$

$$\boldsymbol{P} = \begin{bmatrix} \boldsymbol{P}_1 & \boldsymbol{P}_2 \\ \boldsymbol{P}_2^T & \boldsymbol{P}_3 \end{bmatrix}, Q = \begin{bmatrix} \boldsymbol{Q}_1 & \boldsymbol{Q}_2 \\ \boldsymbol{Q}_2^T & \boldsymbol{Q}_3 \end{bmatrix} \tag{35}$$

Substituting Eq. (32) leads to:

$$\begin{cases}\dot{\boldsymbol{z}}_{i1} = (\boldsymbol{K}\boldsymbol{A}_{21} + \boldsymbol{A}_{11})\boldsymbol{z}_{i1} - ((\boldsymbol{A}_{11} + \boldsymbol{K}\boldsymbol{A}_{21})\boldsymbol{K} - \boldsymbol{A}_{12} - \boldsymbol{K}\boldsymbol{A}_{22})\boldsymbol{y}_i + \boldsymbol{K}\boldsymbol{G}_2(\boldsymbol{T}^{-1}\boldsymbol{z}_i, \boldsymbol{u}_i) + \boldsymbol{G}_1(\boldsymbol{T}^{-1}\boldsymbol{z}_i, \boldsymbol{u}_i) \\ \boldsymbol{z}_{i2} = \boldsymbol{A}_{21}\boldsymbol{z}_{i1} - (\boldsymbol{A}_{21}\boldsymbol{K} - \boldsymbol{A}_{22})\boldsymbol{z}_{i2} + \boldsymbol{G}_2(\boldsymbol{T}^{-1}\boldsymbol{z}_i, \boldsymbol{u}_i) + \boldsymbol{E}_2\boldsymbol{f}_i(t) + \boldsymbol{D}_2\boldsymbol{\Phi}_i(t) \\ \boldsymbol{y}_i = \boldsymbol{z}_{i2}\end{cases} \tag{36}$$

where $\boldsymbol{K} = \boldsymbol{P}_1^{-1}\boldsymbol{P}_2$, $\boldsymbol{z} = col\,(\boldsymbol{z}_1,\boldsymbol{z}_2)$ and $\boldsymbol{z}_1 \in R^{n-p}$.

For Eq. (36), after linear transformation, a sliding mode-based observer was designed, and its stability was proved.

Theorem 1: For the UAV nonlinear system after linear transformation, if

$$\lambda_{\min}(\boldsymbol{Q}_1) > 2L_g \parallel [\boldsymbol{P}_1 \ \boldsymbol{P}_2] \parallel_{\min}$$

is satisfied, the reduced-order observer Eq. (37) will be asymptotically stable on the sliding mode surface.

$$\begin{cases} \dot{\hat{z}}_{i1} = (\boldsymbol{K}\boldsymbol{A}_{21} + \boldsymbol{A}_{11})\hat{z}_{i1} - ((\boldsymbol{A}_{11} + \boldsymbol{K}\boldsymbol{A}_{21})\boldsymbol{K} - \boldsymbol{A}_{12} - \boldsymbol{K}\boldsymbol{A}_{22})\boldsymbol{y}_i \\ \quad + \boldsymbol{K}\boldsymbol{G}_2(\boldsymbol{T}^{-1}\hat{\boldsymbol{z}}_i, \boldsymbol{u}_i) + \boldsymbol{G}_1(\boldsymbol{T}^{-1}\hat{\boldsymbol{z}}_i, \boldsymbol{u}_i) \\ \dot{\hat{z}}_{i2} = \boldsymbol{A}_{21}\hat{z}_{i1} + (\boldsymbol{A}_{22} - \boldsymbol{A}_{21}\boldsymbol{K})\hat{z}_{i2} + \boldsymbol{G}_2(\boldsymbol{T}^{-1}\hat{\boldsymbol{z}}_i, \boldsymbol{u}_i) + \boldsymbol{v}_i \\ \hat{\boldsymbol{y}}_i = \hat{z}_{i2} \end{cases} \tag{37}$$

where

$$\left\| \boldsymbol{G}(\boldsymbol{T}^{-1}\boldsymbol{z}_i, \boldsymbol{u}_i) - \boldsymbol{G}(\boldsymbol{T}^{-1}\hat{\boldsymbol{z}}_i, \boldsymbol{u}_i) \right\| \le L_g \left\| \boldsymbol{T}^{-1}\boldsymbol{z}_i - \boldsymbol{T}^{-1}\hat{\boldsymbol{z}}_i \right\| \tag{38}$$

was obtained by the Lipschitz condition satisfied by the nonlinear term and the sliding mode switching term $\boldsymbol{v}_i$ as follows:

$$\boldsymbol{v}_i = (\left\| \boldsymbol{A}_{22} - \boldsymbol{A}_{21}\boldsymbol{K} \right\| \left\| \boldsymbol{y}_i - \hat{\boldsymbol{y}}_i \right\| + \left\| \boldsymbol{D}_2 \right\| \gamma_1(\boldsymbol{T}^{-1}\hat{\boldsymbol{z}}_i) + \left\| \boldsymbol{E}_2 \right\| \gamma_2 + W)\text{sign}(\boldsymbol{y}_i - \hat{\boldsymbol{y}}_i) \tag{39}$$

where W is a positive real number.

Proof. Suppose $\boldsymbol{e}_1 = z_{i1} - \hat{z}_{i1}$, and $\boldsymbol{e}_y = \boldsymbol{y}_i - \hat{\boldsymbol{y}}_i$, then the error equation can be expressed as:

$$\begin{cases} \dot{\boldsymbol{e}}_1 = (\boldsymbol{A}_{11} + \boldsymbol{K}\boldsymbol{A}_{21})\boldsymbol{e}_1 + \tilde{\boldsymbol{G}}_1 + \boldsymbol{K}\tilde{\boldsymbol{G}}_2 \\ \dot{\boldsymbol{e}}_y = \boldsymbol{A}_{21}\boldsymbol{e}_1 + (\boldsymbol{A}_{22} - \boldsymbol{A}_{21}\boldsymbol{K})\boldsymbol{e}_y + \tilde{\boldsymbol{G}}_2 + \boldsymbol{D}_2\boldsymbol{\Phi}_i(t) + \boldsymbol{E}_2\boldsymbol{f}_i(t) - \boldsymbol{v}_i \end{cases} \tag{40}$$

where

$$\tilde{\boldsymbol{G}}_l = \boldsymbol{G}_l(\boldsymbol{T}^{-1}\boldsymbol{z}_i, \boldsymbol{u}_i) - \boldsymbol{G}_l(\boldsymbol{T}^{-1}\hat{\boldsymbol{z}}_i, \boldsymbol{u}_i),\ l = 1, 2 \tag{41}$$

The designed sliding surface is as follows:

$$\boldsymbol{S} = \left\{ (\boldsymbol{e}_1, \boldsymbol{e}_y) \mid \boldsymbol{e}_y = 0 \right\} \tag{42}$$

Consider the following Lyapunov function:

$$\mathrm{V}_1 = \boldsymbol{e}_1^T \boldsymbol{P}_1 \boldsymbol{e}_1 \tag{43}$$

The derivative of Eq. (43) can be obtained:

$$\dot{\mathrm{V}}_1 = \boldsymbol{e}_1^T [\boldsymbol{P}_1(\boldsymbol{A}_{11} + \boldsymbol{K}\boldsymbol{A}_{21}) + (\boldsymbol{A}_{11} + \boldsymbol{K}\boldsymbol{A}_{21})^T \boldsymbol{P}_1]\boldsymbol{e}_1 + 2\boldsymbol{e}_1^T \boldsymbol{P}_1 [\boldsymbol{I}_{n-p} \quad \boldsymbol{K}][\tilde{\boldsymbol{G}}_1 \quad \tilde{\boldsymbol{G}}_2]^T \tag{44}$$

Eq. (33) is decomposed in the form of Eq. (35), which can be expressed as:

$$\boldsymbol{P}_1(\boldsymbol{A}_{11} + \boldsymbol{K}\boldsymbol{A}_{21}) + (\boldsymbol{A}_{11} + \boldsymbol{K}\boldsymbol{A}_{21})^T \boldsymbol{P}_1 = -\boldsymbol{Q}_1 \tag{45}$$

Combining Eq. (43) and Eq. (44) leads to:

$$\begin{aligned}\dot{\mathrm{V}}_1 &= -\boldsymbol{e}_1^T \boldsymbol{Q}_1 \boldsymbol{e}_1 + 2\boldsymbol{e}_1^T \begin{bmatrix} \boldsymbol{P}_1 & \boldsymbol{P}_2 \end{bmatrix} \begin{bmatrix} \widetilde{\boldsymbol{G}}_1 & \widetilde{\boldsymbol{G}}_2 \end{bmatrix}^T \\ &\le -\boldsymbol{e}_1^T \boldsymbol{Q}_1 \boldsymbol{e}_1 + 2L_g \left\| \boldsymbol{e}_1^T \right\| \left\| \begin{bmatrix} \boldsymbol{P}_1 & \boldsymbol{P}_2 \end{bmatrix} \right\| \left\| \boldsymbol{T}^{-1}(\boldsymbol{z} - \hat{\boldsymbol{z}}) \right\| \\ &\le -\left\| \boldsymbol{e}_1 \right\|^2 \left(\lambda_{\min}(\boldsymbol{Q}_1) - 2L_g \left\| \begin{bmatrix} \boldsymbol{P}_1 & \boldsymbol{P}_2 \end{bmatrix} \right\| \right) \\ &\le 0 \end{aligned} \tag{46}$$

Thus, the system can be stabilized on the sliding surface.

Via the designed observer, the fault was estimated. When the system reaches the sliding mode surface for sliding mode motion,

$$\boldsymbol{e}_y = 0, \dot{\boldsymbol{e}}_y = 0 \tag{47}$$

then Eq. (40) can be changed to:

$$0 = \boldsymbol{A}_{21}\boldsymbol{e}_1 + \tilde{\boldsymbol{G}}_2 + \boldsymbol{D}_2 \boldsymbol{\Phi}_i(t) + \boldsymbol{E}_2 \boldsymbol{f}_i(t) - \boldsymbol{v}_{eq} \tag{48}$$

Because of

$$\lim_{t \to 0} \boldsymbol{e}_1 = 0$$

it can be derived as follows:

$$\boldsymbol{v}_{eq} = \begin{bmatrix} \boldsymbol{D}_2 & \boldsymbol{E}_2 \end{bmatrix} \begin{bmatrix} \boldsymbol{\Phi}_i(t) \\ \boldsymbol{f}_i(t) \end{bmatrix} \tag{49}$$

Suppose there exists $\boldsymbol{M}_d = \begin{bmatrix} \boldsymbol{M}_1 & \boldsymbol{M}_2 \end{bmatrix}^T \in R^{p \times p}$ satisfying the following:

$$\begin{bmatrix} \boldsymbol{M}_1 \\ \boldsymbol{M}_2 \end{bmatrix} \begin{bmatrix} \boldsymbol{D}_2 & \boldsymbol{E}_2 \end{bmatrix} = \begin{bmatrix} \boldsymbol{H}_1 & \boldsymbol{H}_2 \\ \boldsymbol{0} & \boldsymbol{H}_3 \end{bmatrix} \tag{50}$$

Further, combining Eq. (49) and Eq. (50) can yield the following:

$$\boldsymbol{M}\boldsymbol{v}_{eq} = \begin{bmatrix} \boldsymbol{H}_1 & \boldsymbol{H}_2 \\ \boldsymbol{0} & \boldsymbol{H}_3 \end{bmatrix} \begin{bmatrix} \boldsymbol{\Phi}_i(t) \\ \boldsymbol{f}_i(t) \end{bmatrix} \tag{51}$$

Thus, the fault and disturbance can be estimated as:

$$\hat{\boldsymbol{f}}_i(t) = \boldsymbol{H}_3^{-1} \boldsymbol{M}_2 \boldsymbol{v}_{eq} \tag{52}$$

$$\hat{\boldsymbol{\Phi}}_i(t) = \boldsymbol{H}_1^{-1} (\boldsymbol{M}_1 - \boldsymbol{H}_2 \boldsymbol{H}_3^{-1} \boldsymbol{M}_2) \boldsymbol{v}_{eq} \tag{53}$$

where

$$\boldsymbol{v}_{eq} = \frac{\boldsymbol{y}_i - \hat{\boldsymbol{y}}_i}{\epsilon + \left\| \boldsymbol{y}_i - \hat{\boldsymbol{y}}_i \right\|} \left(\left\| \boldsymbol{y}_i - \hat{\boldsymbol{y}}_i \right\| \left\| \boldsymbol{A}_{22} - \boldsymbol{A}_{21}\boldsymbol{K} \right\| + \gamma_2 \left\| \boldsymbol{E}_2 \right\| + \gamma_1 (\boldsymbol{T}^{-1}\hat{\boldsymbol{z}}) \left\| \boldsymbol{D}_2 \right\| + W \right) \tag{54}$$

where ϵ is a very small real number.

A compensation control scheme is presented. From the previous analysis, it is known that the estimation errors of faults and disturbances are bounded and stable. Therefore, a compensation control term was added to the controller in the absence of faults to offset the adverse impact of actuator faults on the UAVs. The fault-tolerant control method can be rewritten as follows:

$$\boldsymbol{u}_i^* = \boldsymbol{u}_i + \boldsymbol{u}_{fi} \tag{55}$$

where

$$\boldsymbol{u}_{fi} = -\boldsymbol{B}^T(\boldsymbol{B}\boldsymbol{B}^T)^{(-1)}(\boldsymbol{D}\hat{\boldsymbol{\Phi}}_i(t) + \boldsymbol{E}\hat{\boldsymbol{f}}_i(t)) \tag{56}$$

4. Experimental Results

Due to the limitations in the number of experimental equipment and venues, three UAVs, including one leader UAV and two wingmen, were subjected to physical verification experiments to verify the effectiveness of the fault-tolerant control method for low-altitude UAV clusters via the reduced-order sliding mode observer and the stability of the entire formation. To ensure the online operation of various complex algorithms, after using the flight control unit for low-altitude control, all UAVs in the experiment were equipped with an ARM-based microcomputer, ODROID-XU4. This computer runs a 64-bit operating system and has an ROS development environment built on it. Most of the communication and data interaction in the project is based on the communication protocol of the ROS. The sensor system used in this experiment is a sensor model more suitable for coverage path planning, which better describes the coverage effect of the sensor for different location areas around it, by quantitatively describing the coverage effect on a certain range of area surrounding the flight path, rather than at a fixed point. When the UAV moves along a certain path, the sensor system will continuously collect the surrounding information, during which the same point will be observed several times. In addition, it is straightforward to optimize the coverage path of the UAV, i.e., a segment of the curve, to calculate the coverage path that can collect the most accurate and reliable position information. The spatial localization system used in the experiments is the OptiTrack system, which consists of a number of infrared cameras distributed on the top around the room to achieve the tracking of UAVs within a defined range. Its infrared cameras are connected to a PC serving as the host computer through an OptiHub integrator, which provides positional information for the indoor target by recognizing the calibration sphere attached to the target. A dual-frequency wireless router was used in this study to set up a local area network to connect all experimental devices. The entire network environment is shown in Fig. 3, which includes both a wired and a wireless local area network. The experimental setup included a leader UAV (Qbot2-L) and two follower UAVs (Qball-X4 and Qbot2-F).

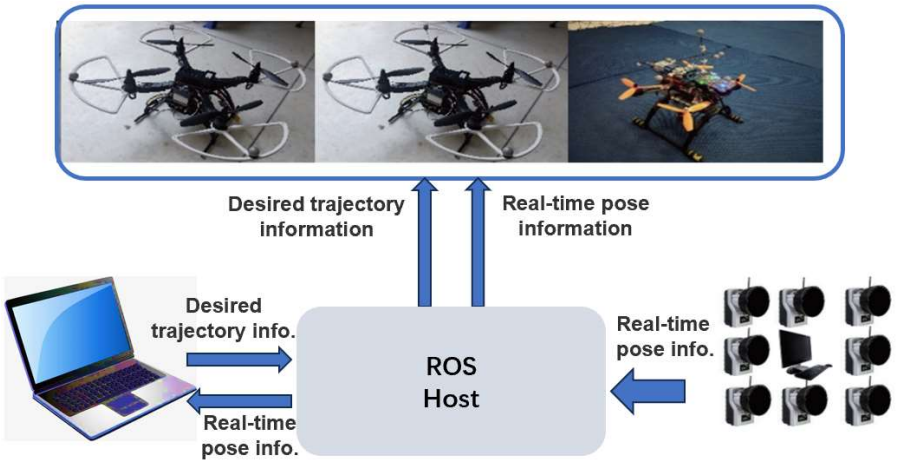

Fig. 3 Low-altitude UAV swarm experimental platform

In considering the failure of a single actuator, the four motors were named separately to distinguish the four motors of the quadrotor. The specific naming method was to take the nose as the forward. The motor inputs were designated as follows: the rear motor as u1, the front as u2, the left as u3, and the right as u4. The fault selection in this compensate is a 10% failure of the rear motor, occurring 35 seconds after the start of the mission. The control parameters were selected as:

$$\boldsymbol{D} = [1, -2.682, 0, 5]^T \tag{57}$$

$$\boldsymbol{F}_1 = [-1.753, -0.0612, 0.1356] \tag{58}$$

$$\boldsymbol{F}_2 = \begin{bmatrix} 0.1287 & -1.4021 & -3.1981 \\ -0.0112 & -4.1372 & -0.0498 \end{bmatrix} \tag{59}$$

$$\boldsymbol{H} = \begin{bmatrix} -2.682 & -1.093 & 0.2534 \\ 0 & 0.416 & -4.211 \\ 0 & -143.234 & 0.4532 \end{bmatrix} \tag{60}$$

4.1 Single Actuator Failure

It can be seen from Fig. 4 that when the fault occurs, because the rear motor fails by 10%, the rear motor is facing the positive direction of the *z*-axis. Therefore, the positive direction of the *z*-axis decreases, resulting in a decrease in the pitch angle. The observer will compensate for the estimated fault size in the controller to return the UAV to the original path. The pitch angle is maintained at the original angle and the pitch angle control command increases rapidly. After about 8 seconds, the UAV returns to the proper path, and the pitch angle control command returns to zero. It can be seen from the OptiTrack curve that the actual pitch angle is not greatly affected. In addition, it can be seen that the effectiveness

of the reduced-order sliding mode observer and the fault-tolerant controller is evident and will be more intuitively reflected in the subsequent trajectory diagram.

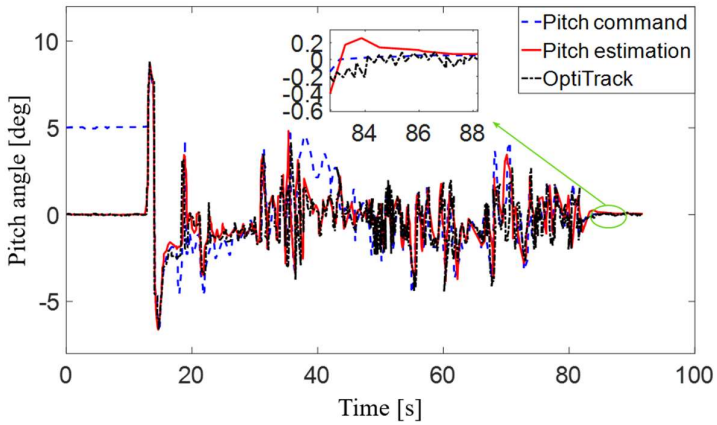

Fig. 4 Pitch angle tracking when a single actuator fails

Remark 1: Too many transitions can be seen in the results. Some transitions are inevitable in the dynamic adjustment of UAV systems, while others are caused by external interference noise. They can be eliminated by increasing the hardware's anti-interference ability.

As it can be seen in Fig. 5, the roll angle is almost not affected by the failure of the rear motor. The roll angle command only changes for a split second at 35 seconds, but the whole is not affected, which is consistent with the theoretical situation.

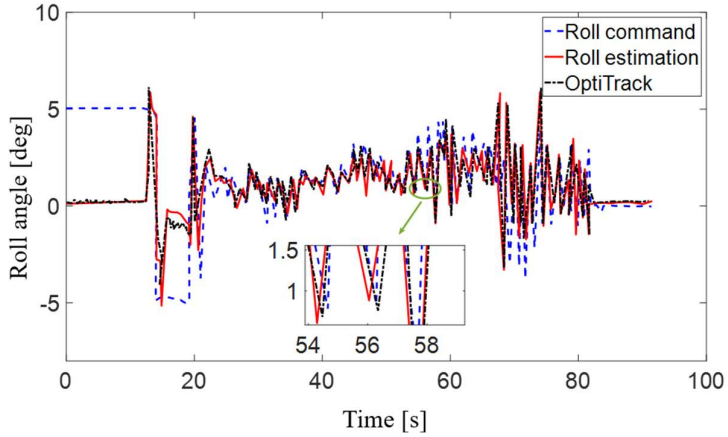

Fig. 5 Roll angle tracking when a single actuator fails

Fig. 6 shows that, at 35 seconds, due to the failure of the rear motor by 10%, the lift provided is reduced. Therefore, the height is affected and slightly reduced. But within two or three seconds, the height is adjusted back to the set 0.7 meters, which shows the effectiveness of the height control method.

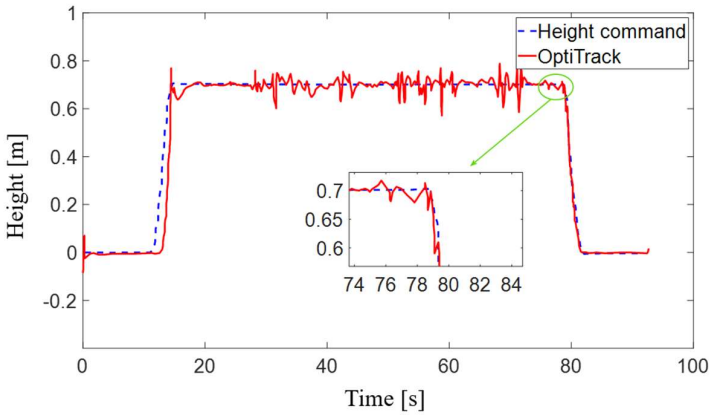

Fig. 6 Height tracking when a single actuator fails

Diagrams in Figs. 7-8 demonstrate that the reduced-order sliding mode observer can basically estimate the size of the fault. But due to the large fluctuation of noise, the observer estimates the fault quickly and can quickly compensate for the estimated value into the motor control instruction of the corresponding channel, where the motor command ordinate is the percentage of the full speed of the motor rotor. It should also be pointed out that in Figs. 4 to 8, approximately the first 15 seconds are used by the UAV to take off to the departure site. Therefore, all angles are still adjusted.

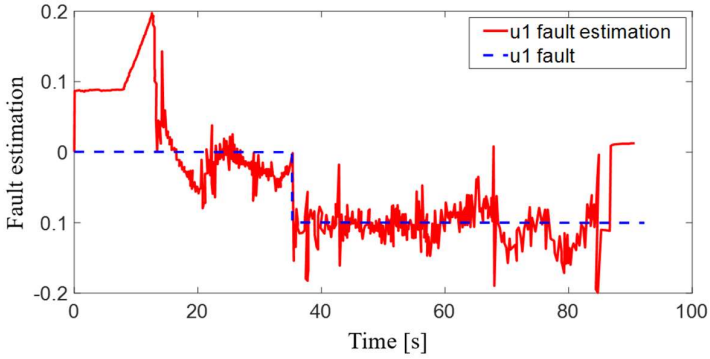

Fig. 7 Fault estimation when a single actuator fails

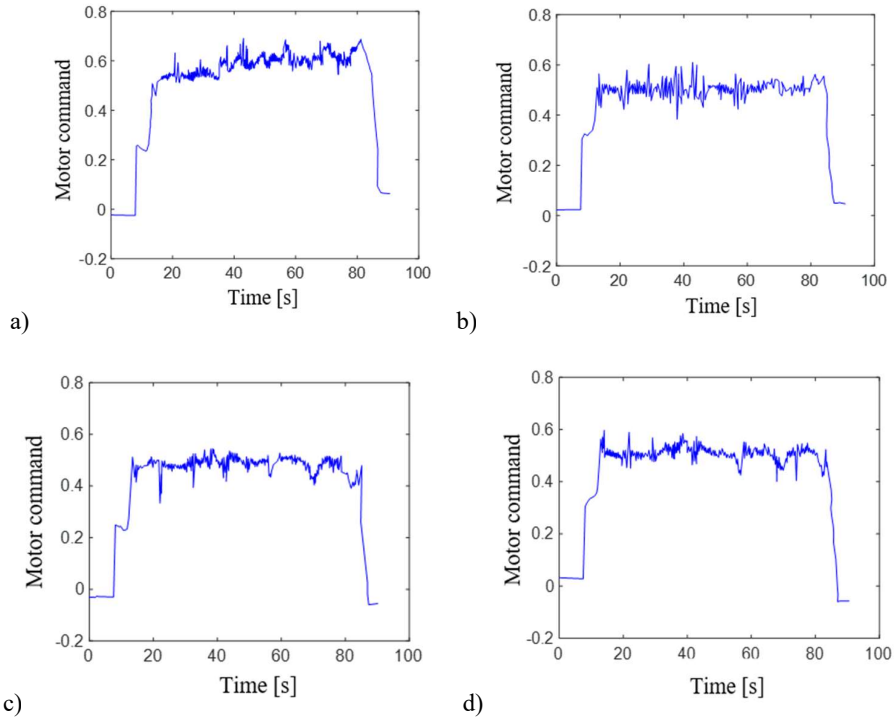

Fig. 8 Actuator command when a single actuator fails: a) u1; b) u2; c) u3; d) u4

Qbot2-L and Qbot2-F are two ground-based two-degree-of-freedom unmanned robots, with Qball-X4 being a quadrotor UAV. Qbot2-L acts as the leader, while Qbot2-F and Qball-X4 serve as wingmen, building a formation.

Fig. 9 presents top-down views, which are the projection views of the formation on the ground. The objective is for the wingmen to always follow the leader, even if a malfunction occurs. In Fig. 9, Qbot2-L starts from (0,0) with a route of (0.75, -0.75), (-0.75, -0.75), (-0.75, 0.75), and (0.75, 0.75). Meanwhile, Qbot2-F begins from (0.1, 1) and Qball-X4 from (0.8, 0.45), both following Qbot2-L. When Qball-X4, the UAV, reaches (0.3, -0.9), its motor u1 malfunctions, causing it to stray from the formation. However, after approximately 0.4 meters, around the location (-0.1, -0.9), it resumes its tracking of the leader, Qbot2-L, to the designated position. This scenario demonstrates the effectiveness of the proposed fault diagnosis and fault-tolerant control scheme. The fault has little impact on the UAVs. After about 0.4 meters, UAVs track the long aircraft to the designated position again, and the entire formation is still stable, which shows the effectiveness and practical application value of the fault diagnosis and the fault-tolerant control scheme designed in this topic.

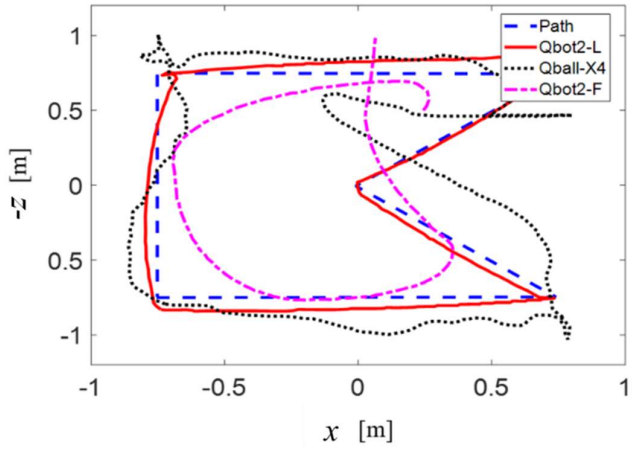

Fig. 9 Top view trajectory when a single actuator fails

4.2 Failure of Two Actuators

On the basis of the original rear motor failure, the right motor in the asymmetrical position also fails at 49 seconds, and the fault form is u4 f = 105%*u4, and the specific experimental results are shown below.

As can be seen from Figs. 10-11, the pitch angle at 35 seconds is similar to that of a single fault in Fig. 5, and the pitch angle control command changes only briefly at 49 seconds. At 49 seconds, the roll angle decreases because the output of the right motor suddenly becomes larger and the right motor is in the negative direction of the *x*-axis. Therefore, the roll angle decreases and the roll angle control command increases rapidly.

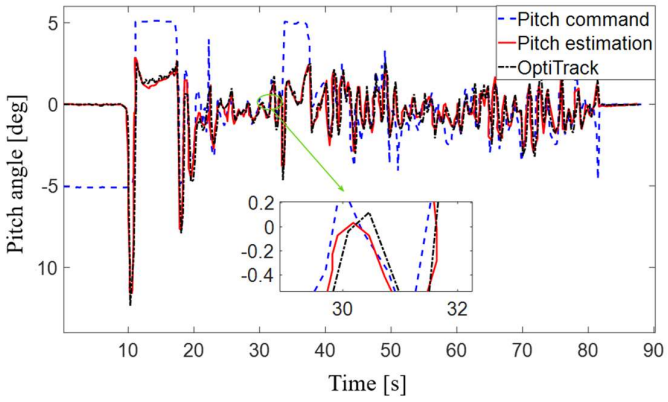

Fig. 10 Pitch angle tracking when two actuators fail

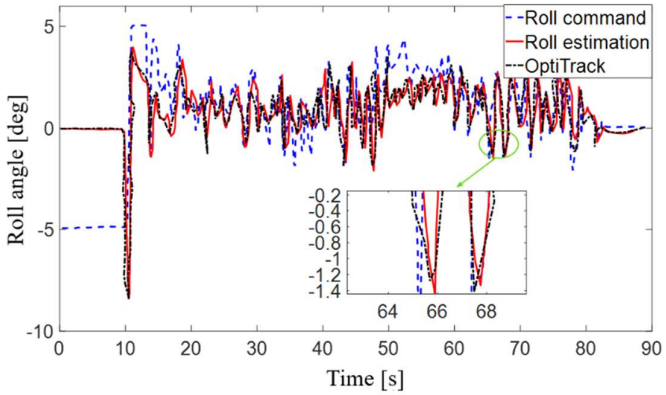

Fig. 11 Roll angle tracking when two actuators fail

In Fig. 12, the height decreases slightly at 35 seconds and increases slightly at 49 seconds, but both quickly adjust back to 0.7 meters, showing that the control is still ideal in the event of actuator failure of the motor in two asymmetrical positions.

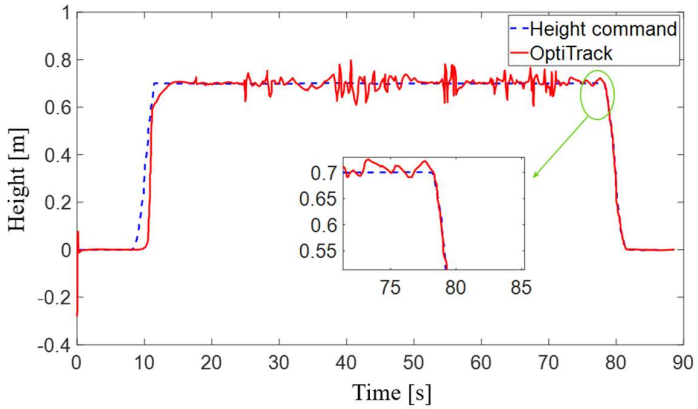

Fig. 12 Height tracking when two actuators fail

It can be seen from Figs. 13-14 that the adaptive sliding mode observer can do better fault estimation for both faults. However, compared with the situation of a single motor failure, the effect of fault estimation is slightly reduced, and the control instructions of the corresponding two motors are slightly slowed down when compensating for the fault, but this is also related to factors such as battery voltage during the experiment. Overall, the fault-tolerant controller and the adaptive sliding mode observer reach the pre-target, which shows that the fault diagnosis scheme is still ideal in dealing with multiple faults.

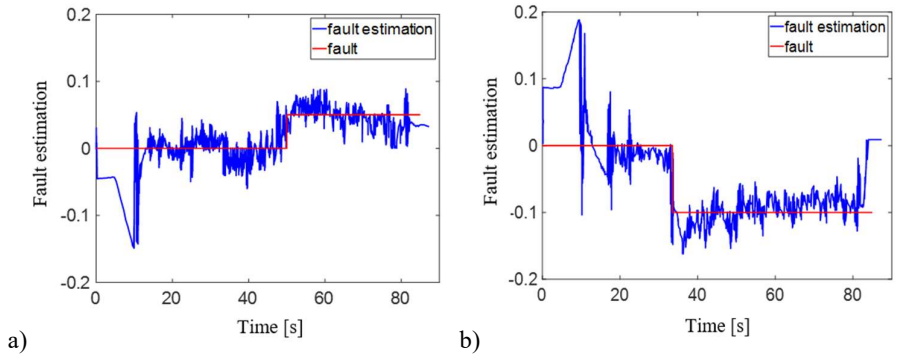

Fig. 13 Fault estimation when two actuators fail: a) u2; b) u4

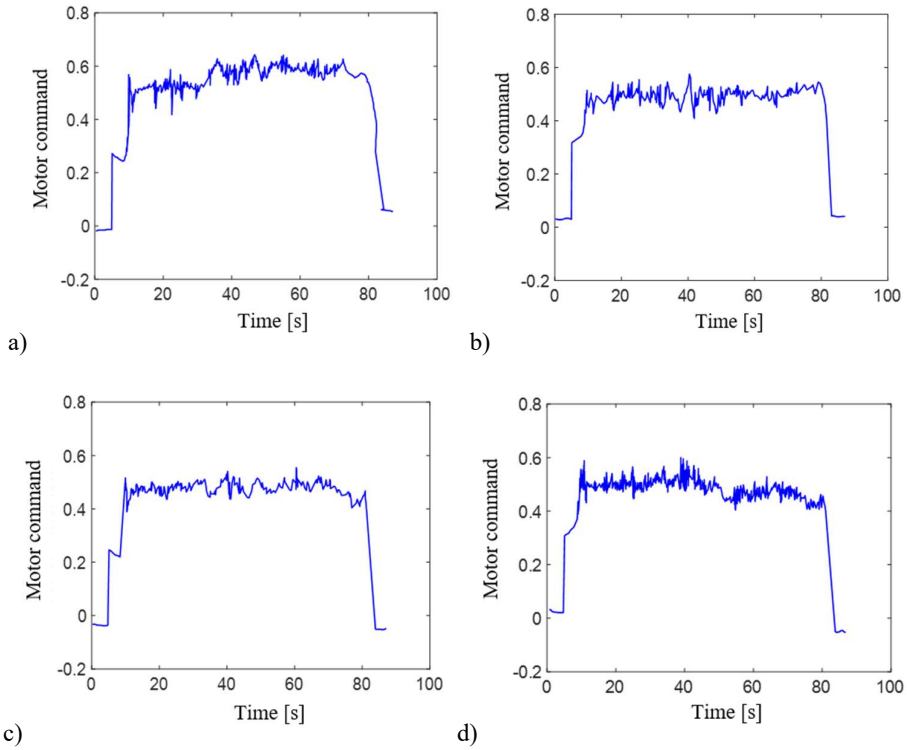

Fig. 14 Actuator commands when two actuators fail: a) u1; b) u2; c) u3; d) u4

Qbot2-L acts as the leader, while Qbot2-F and Qball-X4 serve as wingmen, forming a formation. Fig. 15 presents top-down views, which are the projection views of the formation on the ground. The objective is for the wingmen to always follow the leader,

even if a malfunction occurs. In Fig. 15, Qbot2-L starts from (0, 0) with the same route as in Fig. 9. Meanwhile, Qbot2-F begins from (-0.5, 0.7) and Qball-X4 from (-0.4, 0), both following Qbot2-L. It can be observed that the u1 failure occurs at point (0.2, -1), and the u4 failure occurs at point (-0.7, -0.6). Furthermore, both failures occur simultaneously. It is evident that the flight quality of the UAVs decreases. Due to the adoption of the directed graph communication topology in this formation, the leader UAV (Qbot2-L) does not receive information from the follower UAV (Qball-X4) or wait for adjustments from it. To catch up with the leader, the follower directly flows in a curve at point (-0.75, -0.75), instead of hovering in the air waiting for the Qbot2-L to change direction, as it would have done without failure. Overall, the entire formation is still able to maintain a good formation even in the latter half, where both failures occur simultaneously. The failure of the UAV Qball-X4 does not affect the tracking of the Qbot2-F on the other side. This demonstrates that the formation scheme studied in this research, along with the fault diagnosis and the fault-tolerant control scheme for UAV swarms, has a certain engineering application value.

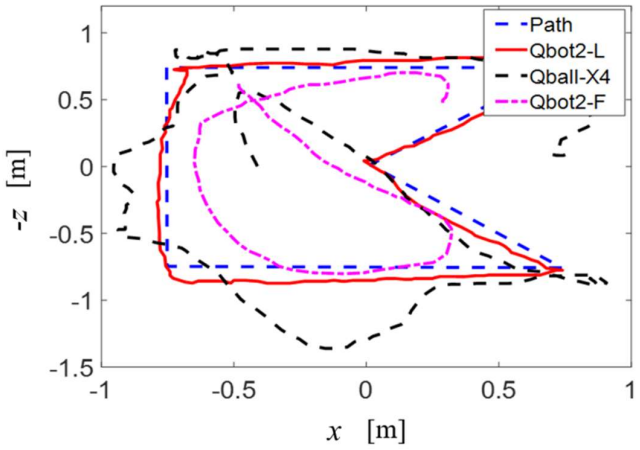

Fig. 15 Top view trajectory when two actuators fail

5. CONCLUSION

This study proposed a fault-tolerant control strategy tailored for low-altitude UAV swarms subject to actuator faults. A reduced-order sliding mode observer was designed to enable real-time fault diagnosis, with the estimated fault information actively fed into a sliding mode tracking controller to achieve timely compensation. This structure enhances both the robustness and real-time responsiveness of the system under actuator failure conditions. Without the need for additional fault-specific sensors, actuator faults were reconstructed online using only the available system state information. In particular, the proposed reduced-order observer significantly improved computational efficiency while maintaining diagnostic accuracy, which is especially beneficial for embedded platforms with limited computational resources. The overall stability of the closed-loop system, incorporating the observer and controller, was rigorously established using the Lyapunov-

based methods. The proposed control scheme was further validated through experimental tests on a custom-built low-altitude UAV swarm platform, demonstrating effective performance under both single- and dual-actuator fault scenarios. This work focuses on the fault-tolerant performance of the control system. In future research, further consideration will be given to the robust performance, such as the robustness of controller gains (e.g., sliding mode gain, sign function bounds).

REFERENCES

1. Spanogianopoulos, S., Ahiska, K., 2024, *Formation solution for heterogeneous swarm of UAVs and MAVs in crowded environment*, 2024 10th International Conference on Control, Decision and Information Technologies (CoDIT), Vallette, Malta, pp. 158-163.
2. Silva, L.S., Santos, D.A., 2020, *Fast nonsingular terminal sliding mode flight control for multirotor aerial vehicles*, IEEE Transactions on Aerospace and Electronic Systems, 56(6), pp. 4288-4299.
3. Seo, J., Kim, Y., Kim, S., Tsourdos, A., 2017, *Collision avoidance strategies for unmanned aerial vehicles in formation flight*, IEEE Transactions on Aerospace and Electronic Systems, 53(6), pp. 2718-2734.
4. Shahzad, M.M., Asad, M.H., Haris, M., Munawar, H., Yousaf, M.H., 2023, *Formation control and sub-swarm generation of multirotor UAVs*, 2023 International Conference on Robotics and Automation in Industry (ICRAI), Peshawar, Pakistan, pp. 1-7.
5. Volovoda, T., 2024, *Swarm intelligence for UAV*, 2024 IEEE 7th International Conference on Actual Problems of Unmanned Aerial Vehicles Development (APUAVD), Kyiv, Ukraine, pp. 313-316.
6. Kim, M., Lee, H., Hwang, S., Debbah, M., Lee, I., 2024, *Cooperative multiagent deep reinforcement learning methods for UAV-aided mobile edge computing networks*, IEEE Internet of Things Journal, 11(23), pp. 38040-38053.
7. Amhaz, A., Elhattab, M., Sharafeddine S., Assi, C., 2024, *UAV-assisted cooperative downlink NOMA: deployment and resource allocation*, IEEE Transactions on Vehicular Technology, 73(9), pp. 13651-13664.
8. Singh, C.K., Upadhyay, P.K., Lehtomäki, J., Juntti, M., 2023, *Performance analysis with deep learning assay for cooperative UAV-borne IRS NOMA networks under non-ideal system imperfections*, IEEE Transactions on Vehicular Technology, 73(1), pp. 1065-1083.
9. Dong, X.W., Hua, Y.Z., Zhou, Y., Ren, Z., Zhong, Y.S., 2018, *Theory and experiment on formation-containment control of multiple multirotor unmanned aerial vehicle systems*, IEEE Transactions on Automation Science and Engineering, 16(1), pp. 229-240.
10. Liao, F., Teo, R., Wang, J.L., Dong, X.X., Lin F., Peng, K., 2017, *Distributed formation and reconfiguration control of VTOL UAVs*, IEEE Transactions on Control Systems Technology, 25(1), pp. 270-277.
11. Kang, S.M., Park, M.C., Ahn, H.S., 2017, *Distance-based cycle-free persistent formation: global convergence and experimental test with a group of quadcopters*, IEEE Transactions on Industrial Electronics, 64(1), pp. 380-389.
12. Belkadi, A., Abaunza, H., Ciarletta, L., Castillo, P., Theilliol, D., 2019, *Design and Implementation of Distributed Path Planning Algorithm for a Fleet of UAVs*, IEEE Transactions on Aerospace and Electronic Systems, 55(6), pp. 2647-2657.
13. Yang, Q.Q., Chen, J., Peng, Y., 2023, *Unmanned aerial vehicle trajectory planning and power control algorithm based on deep deterministic policy gradient*, Journal of Beijing University of Posts and Telecommunications, 46(3), pp. 43-48.
14. Liu, J.Y., Jiang, F.B., Peng, Y.B., Dong, L., 2024, *Multi-objective optimization for unmanned aerial vehicles trajectory model based on decomposition and trajectory search*, Journal of Computer Applications, 43(12), pp. 3806-3815.
15. Gupta, L., Jain, R., G. Vaszkun, G., 2016, *Survey of important issues in UAV communication networks*, IEEE Communications Surveys & Tutorials, 18(2), pp. 1123-1152.
16. Lin, H.W., Zhao, B., Liu, D.R., Alippi, C., 2020, *Data-based fault tolerant control for affine nonlinear systems through particle swarm optimized neural networks*, IEEE/CAA Journal of Automatica Sinica, 7(4), pp. 954-964.
17. Patton, R.J., Frank, P.M., Clark, R.N., 2000, *Issues of Fault Diagnosis for Dynamic Systems,* Spring-Verlag, London.
18. Hasanshahi, M., Ahmadi, A.A., Amjadifard, R., 2019, *Robust fault tolerant position tracking control for a quadrotor UAV in presence of actuator faults,* 2019 6th International Conference on Control, Instrumentation and Automation (ICCIA), Sanandaj, Iran, pp. 1-6.

19. Yang, X.F., Hu, X.B., Ye, H., Liu, W., Shen, H., 2023, *Fraction-order MRAC method based fault tolerant control for plant protection UAV with actuator failure and uncertainty*, International Journal of Control, Automation and Systems, 21(8), pp. 2623-2633.
20. Liu, K., Wang, R.J., Zheng, S.J., Dong, S.F., Sun, G.W., 2022, *Fixed-time disturbance observer-based robust fault-tolerant tracking control for uncertain quadrotor UAV subject to input delay*, Nonlinear Dynamics, 107(3), pp. 2363-2390.
21. Wang, Z.F., Yu, J.G., Lin, S.J., Dong, J.G., Yu, Z., 2019, *Distributed robust adaptive fault-tolerant mechanism for quadrotor UAV real-time wireless network systems with random delay and packet loss*, IEEE Access, 7, pp. 134055-134062.
22. Liu, K., Wang, R.J., Wang, X.D., Wang, X.X., 2021, *Anti-saturation adaptive finite-time neural network based fault-tolerant tracking control for a quadrotor UAV with external disturbances*, Aerospace Science and Technology, 115, 106790.
23. Yu, X., Li, P., Zhang, Y.M., 2017, *Fault-tolerant control design against actuator faults with application to UAV formation flight*, 2017 36th Chinese Control Conference (CCC), pp. 7167-7171.
24. Reppa, V., Polycarpou, M.M., Panayiotou, C.G., 2015, *Distributed sensor fault diagnosis for a network of interconnected cyberphysical systems*, IEEE Transactions on Control of Network Systems, 2(1), pp. 11-23.
25. Wu, S.T., 2013, Flight Control System. Beihang University Press.
26. Kumar, S., Kumar, A., Lee, D.G, 2022, *Semantic segmentation of UAV images based on transformer framework with context information*, Mathematics, 10(24), 4735.
27. Kurdi, H., AlDaood, M.F., Al. Megren, S., Aloboud, E., Aldawood, A.S., Youcef-Toumi, K., 2019, *Adaptive task allocation for multi-UAV systems based on bacteria foraging behaviour*, Applied Soft Computing, 83, pp. 105643-105661.
28. Aljalaud, F., Kurdi, H., Youcef-Toumi, K., 2023, *Autonomous multi-UAV path planning in pipe inspection missions based on booby behavior*, Mathematics, 11(9), 2092.
29. Liu, Z.X., Yu, X., Yuan, C., Zhang, Y.M., 2015, *Leader-follower formation control of unmanned aerial vehicles with fault tolerant and collision avoidance capabilities*, International Conference on Unmanned Aircraft Systems, Denver, USA, pp. 1025-1030.